Lattice dynamics of the ordered vacancy compound HgIn2 square operator Te4

J. Phys. C: Solid State Phys., Vol. 9, 1976. Printed in Great Britain. © 1976

Lattice dynamics of the ordered vacancy compound $HgIn_2\square Te_4$

A Miller†, D J Lockwood‡, A MacKinnon† and D Weaire†
†Department of Physics, Heriot-Watt University, Edinburgh, EH14 4AS, Scotland
‡Department of Physics, University of Edinburgh, Edinburgh EH9 3JZ, Scotland

Received 30 March 1976

Abstract. $HgIn_2\square Te_4$ has a structure which may be regarded as being derived from that of zincblende by the incorporation of an ordered array of vacancies. The $k = 0$ vibrational modes of this compound have been studied using infrared reflectivity and Raman scattering measurements, the latter using Brewster-angle geometry. A semi-empirical theoretical model of the Keating type achieves a reasonable fit to the observed mode frequencies as well as the elastic constant data of Saunders and Seddon, and is used to predict dispersion relations. Qualitative features of the spectrum related to the role of the vacancy are discussed.

1. Introduction

Among the various families of tetrahedrally bonded compound semiconductors, there are some in which the crystal structure may be regarded as being derived from zincblende (or, in some cases, wurtzite) by the incorporation of an ordered array of vacancies. An example of such a compound is $HgIn_2\square Te_4$, the symbol $\square$ denoting the vacancy. Note that if the vacancy is treated as an atom of zero valence, then the Grimm–Somerfeld rule, which demands an average of four valence electrons per atom, is obeyed (Parthé 1964).

The above compound is one of a series intermediate between HgTe, in which every tetrahedral site is filled, and In_2Te_3 (or $In_2\square Te_3$), in which one in every six sites in unfilled. This series has been chosen by Saunders and Seddon (1970, 1976) for an investigation of the influence of the vacancies on various properties, including elastic constants.

We have chosen $HgIn_2\square Te_4$ for an investigation of lattice vibrational properties since it has a comparatively simple structure with seven atoms (i.e. eight tetrahedral sites) per unit cell (see figure 1). The vacancies form a body-centred tetragonal lattice. There has been some uncertainty in the past regarding the arrangement of Hg and In atoms. One possibility (Parthé 1964, Hahn *et al* 1955) may be called *defect chalcopyrite*, because of its close relationship to the chalcopyrite structure. This has symmetry $I\bar{4}$. The second possibility (Saunders and Seddon 1976) has symmetry $I\bar{4}2m$ and may be appropriately dubbed *defect stannite* to indicate its relationship to the stannite structure. Recent work on our material has firmly established the Laué group to be $4/mmm$ (F N Laird and R J Nelmes, private communication) so we believe the $I\bar{4}2m$ space group to be the correct alternative for our samples, figure 1. There is very little tetragonal compression, the axial ratio being close to its ideal value of 2·0.

We have performed infrared reflectivity and Raman scattering measurements, which, together with Saunders and Seddon's results for the elastic constants, furnish a considerable body of data which one may attempt to fit with appropriate semi-empirical models.

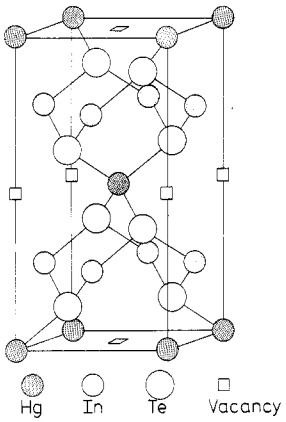

Figure 1. $HgIn_2\square Te_4$, $I\bar{4}2m$ structure.

In the only comparable previous work, that of Finkman *et al* (1975) on In_2Te_3, the attempt at analysis was in terms of the *folding* of dispersion relations appropriate to zincblende into the smaller Brillouin zone of the compound. This procedure, which has been widely used for the chalcopyrite compounds (in which there are no vacant sites), is highly questionable in the present case. It is, however, an interesting first approximation, and one of the calculations which we have performed is intended to indicate how the folded zincblende spectrum evolves when the mass and force constants associated with an ordered array of atoms are continuously reduced to zero to form a defect structure. A semi-empirical Keating model (i.e. bond bending and stretching forces only) was used. In addition, we have performed a calculation of the $\boldsymbol{k} = 0$ modes and elastic constants of $HgIn_2\square Te_4$ in the defect stannite structure, $I\bar{4}2m$. In this way, an approximate fit has been made to all of the available data using adjustable force constants.

Dispersion relations have been calculated using these force constants. While it would be difficult to investigate the dispersion relations for this particular compound by conventional neutron scattering techniques, there are closely related compounds with the $I\bar{4}2m$ and $I\bar{4}$ structures for which such a measurement should be feasible.

2. Group theory and selection rules

The $HgIn_2\square Te_4$ crystal used in this work has a body-centred tetragonal structure with the symmorphic space group $I\bar{4}2m$. There is one formula unit, i.e. 7 atoms, per unit cell, corresponding to 21 degrees of freedom. The character table for lattice vibrational modes at $\boldsymbol{k} = 0$ is given in table 1. This shows that the 18 optical modes may be associated with 5 irreducible representations in the combination $2A_1 + 1A_2 + 2B_1 + 3B_2 + 5E$. The E modes are doubly degenerate. All but the A_2 modes are Raman-active, while only the B_2 and E modes are infrared-active, having dipole moments in the z direction and in

Table 1. Character table for $k = 0$ modes of defect stannite with point group $\bar{4}2m$.

	E	C_2	$2S_4$	$2C_2'$	$2\sigma_d$	N_{opt}	N_{ac}	Activity	Symmetry
A_1	1	1	1	1	1	2		Raman	$x^2 + y^2, z^2$
A_2	1	1	1	−1	−1	1		Inactive	
B_1	1	1	−1	1	−1	2		Raman	$x^2 - y^2$
B_2	1	1	−1	−1	1	3	1	IR, Raman	z; xy
E	2	−2	0	0	0	5	1	IR, Raman	(x, y); (xz, yz)

the xy plane, respectively. This should give rise to TO–LO splittings for B_2 and E vibrational energies. The Raman tensors for the $\bar{4}2m$ point group are

$$A_1 \quad \begin{bmatrix} a & . & . \\ . & a & . \\ . & . & b \end{bmatrix} \qquad B_1 \quad \begin{bmatrix} c & . & . \\ . & -c & . \\ . & . & . \end{bmatrix} \qquad B_2\,(z) \quad \begin{bmatrix} . & d & . \\ d & . & . \\ . & . & . \end{bmatrix} \qquad E\,(x, y) \quad \begin{bmatrix} . & . & . \\ . & . & e \\ . & e & . \end{bmatrix} \quad \begin{bmatrix} . & . & e \\ . & . & . \\ e & . & . \end{bmatrix}.$$

The defect stannite structure ($I\bar{4}2m$) is closely related to the stannite ($I\bar{4}2m$), chalcopyrite ($I\bar{4}2d$) and defect chalcopyrite ($I\bar{4}$) structures. It is therefore worthwhile making some group theoretical comparisons. All four structures are derived from zincblende by an ordering of different species of atom on the cation sublattice. On the anion sublattice, identical atoms occupy all sites. All four structures are body-centred tetragonal and therefore have the same Brillouin zone, which is related to that of the corresponding zincblende structure, as shown in figure 2 for the case of the ideal axial ratio ($c/a = 2{\cdot}0$).

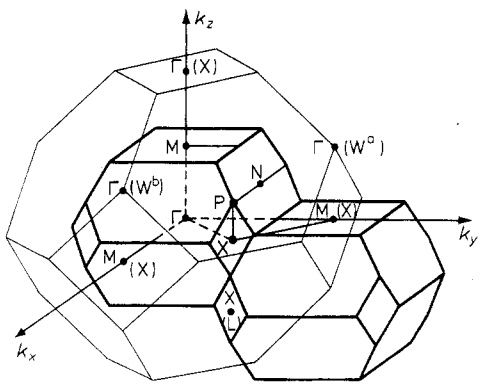

Figure 2. Face-centred cubic and body-centred tetragonal Brillouin zones for $c = 2a$. Symmetry lines are

Γ–M: Λ(00α)	X–M: Y
Γ–M: Σ(α00)	X–P: W
Γ–X: Δ(αα0)	P–N: Q.

Face-centre cubic symmetry points are shown in parenthesis.

It can be seen that the Γ(000), X(001), $W^a(01\frac{1}{2})$ and $W^b(10\frac{1}{2})$ points of zincblende all correspond to Γ(000) of the smaller Brillouin zone. The notation of figure 2 follows Lax (1974).

Chalcopyrite and stannite structures have 8 atoms per unit cell and have the same point group, $\bar{4}2m$. There are thus 21 optical zone-centre modes. In the case of chalcopyrite, these occur in the combination $1A_1 + 2A_2 + 3B_1 + 3B_2 + 6E$ and may be individually associated with Γ-, X- and W-point phonons of zincblende if the masses and force constants are similar in both structures. In particular, X_1, X_3 and X_5 zincblende phonons have A_2, B_1 and E irreducible representations in chalcopyrite, respectively. This association, although somewhat obscured in practice by large differences in masses and force constants, has proved invaluable in the qualitative interpretation of spectra for chalcopyrite crystals (Holah *et al* 1974).

The same would be true of the quaternary stannite structure (e.g. Cu_2FeSnS_4) if the cation masses and force constants were similar. In this case the space group is symmorphic and C_2' and σ_d operations do not have a non-primitive lattice translation associated with them, as in chalcopyrite. Thus X_1, X_3 and X_5 zincblende phonons have A_1, B_2 and E irreducible representations, respectively, and the zone-centre phonons comprise $2A_1 + 1A_2 + 2B_1 + 4B_2 + 6E$.

In order to consider the effect of the reduction in the number of atoms in the defect stannite unit cell, one may imagine the I_2–II–IV–VI_4 stannite structure with the group IV atoms missing. This reduces the number of degrees of freedom by three, with the effect that a B_2 and a doubly-degenerate E mode are lost. In the case of the defect chalcopyrite structure, the removal of the atom would reduce the symmetry to $I\bar{4}$. The 18 optical zone-centre modes then comprise $3A + 5B + 5E$ representations, all of which are Raman-active with the B and E modes infrared-active.

3. Infrared reflectivity

A Bridgman-grown single crystal of $HgIn_2\square Te_4$ of size $10 \times 5 \times 2{\cdot}4\,mm^3$ was kindly supplied by T Seddon and G Saunders, University of Durham. It was cut with a large (100) face and a smaller (001) edge. The final surface preparation for the infrared and Raman measurements was with 1 μm diamond powder on paper backed by flat glass, and the orientation checked by the Laué x-ray back-reflection technique.

The infrared reflectivity measurements were made at room temperature on a Beckman–RIIC FS 720 interferometer in the range 40–400 cm^{-1}. The reflectance module allowed an angle of incidence of 10°; this does not introduce a significant error into the analysis, which assumed normal-incidence Fresnel equations. A grid polarizer was used to polarize the incident radiation parallel and perpendicular to the crystal *c* axis. Reflectance measurements were made from both (100) and (001) faces; the spectral resolution was 4 cm^{-1}.

Figures 3(*a*) and (*b*) show the infrared reflectivity results for radiation polarized parallel (B_2 modes) and perpendicular (E modes) to the *c* axis. Two strong oscillators can be seen in both cases; those with B_2 irreducible representations are sharper and at slightly higher energies than those with E representations.

The data was analysed by combining the Fresnel equation for reflection

$$R = \left| \frac{[\epsilon(\nu)]^{1/2} - 1}{[\epsilon(\nu)]^{1/2} + 1} \right|^2 \tag{1}$$

with an independent harmonic oscillator equation for the dielectric constant

$$\epsilon(\nu) = \epsilon'(\nu) + i\epsilon''(\nu) = \epsilon_\infty + \sum_{j=1}^{2} \frac{S_j}{\nu_j^2 - \nu^2 - i\gamma_j\nu} \tag{2}$$

in a least-squares fitting computer program (Peckham 1970). $\nu_j(cm^{-1})$, $S_j(cm^{-2})$ and $\gamma_j(cm^{-1})$ are the resonant frequency, strength and damping factor, respectively, of the jth oscillator, and ϵ_∞ is the high-frequency dielectric constant due to electronic contributions and is also allowed to vary in the computer fitting. The calculated real and imaginary

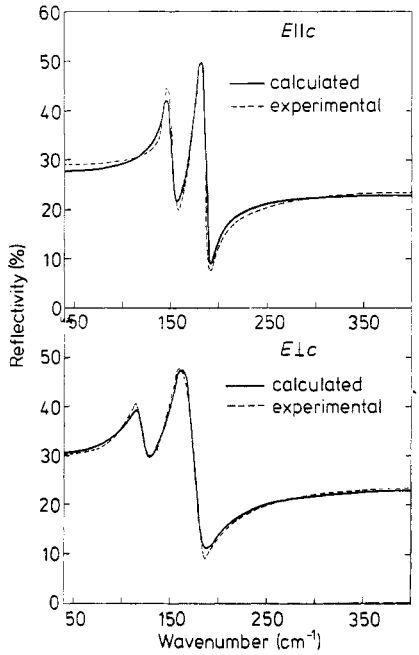

Figure 3. Infrared reflectivity for B_2 and E modes and classical oscillator dispersion fits.

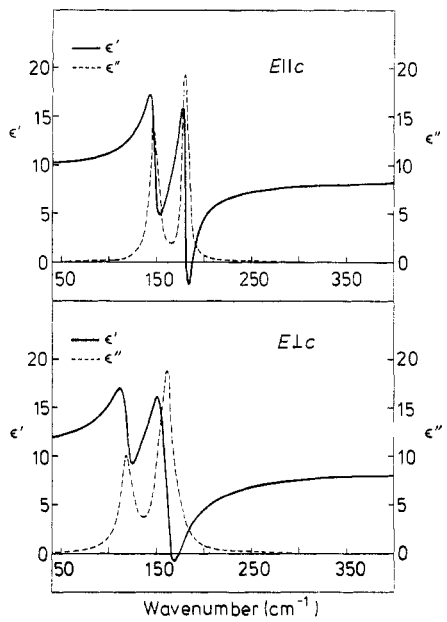

Figure 4. Calculated real and imaginary parts of the dielectric constants for B_2 and E modes.

parts of the dielectric constants are shown in figures 4(*a*) and (*b*). The maximum values of $\epsilon''(\nu)$ are close to the resonant frequency, ν_j, associated with the TO frequencies. The values of the related longitudinal optical frequencies are obtained when $\epsilon'(\nu) = 0$. Where $\epsilon'(\nu)$ does not reach zero, the minimum value is used. Table 2 gives a compilation of the infrared results for the observed B_2 and E modes. The low-frequency dielectric constants were calculated using the Lyddane–Sachs–Teller (1941) relationship.

4. Raman scattering

The Raman measurements were carried out on a Spex 1400 plus TTM triple-grating monochromator with a thermoelectrically-cooled RCA C31034A photomultiplier detector. The spectrometer and detection system were under automatic control (Arthur and Lockwood 1974) and produced the spectrum in a digital form suitable for direct

Table 2. Experimental and calculated results for $HgIn_2\square Te_4$.

Irred. rep. (§ 2)	Infrared (§ 3)				Raman (§ 4)		Calculated (§ 5)
					ν (cm^{-1})		ν (cm^{-1})
A_1 (Γ_1)	Inactive				100		99
					132		140
A_2 (Γ_2)	Inactive				Inactive		114
B_1 (Γ_3)	Inactive				~50		57
					155		158
	ν_{TO}(cm^{-1})	ν_{LO}(cm^{-1})	S(cm^{-2})	γ(cm^{-1})	ν_{TO}	ν_{LO}	ν_{TO}
	—					74	58
B_2 (Γ_4)	147	153	$2{\cdot}1 \times 10^4$	10·2	—	152	139
	180	184	$2{\cdot}2 \times 10^4$	6·6	184	189	181
$\epsilon_\infty = 8{\cdot}53$							
$\epsilon_{(0)} = 9{\cdot}64$							
	—					42	50
	—					61	57
E (Γ_5)	118	127	$1{\cdot}6 \times 10^4$	15·5	122	—	132
	160	169	$5{\cdot}2 \times 10^4$	18·4	162	—	160
	—	—			181	188	179
$\epsilon_\infty = 8{\cdot}57$							
$\epsilon_{(0)} = 11{\cdot}06$							

processing by a large computer. The band gap of $HgIn_2\square Te_4$ is at about 0·9 eV, and thus the crystal is opaque to the visible wavelengths produced by the common laser sources. Therefore, the Raman spectrum was measured in reflection. In initial experiments using back-reflection techniques, various laser lines were tried in order to determine the most suitable exciting frequency. The 488·0 and 514·5 nm lines of the argon laser were heavily absorbed by the crystal and no Raman spectrum could be observed; the He–Ne 632·8 nm laser line and the 568·2, 647·1, 676·4, 752·5 and 799·3 nm lines of the krypton laser produced a weak Raman signal. Contrary to expectation, the longer-wavelength lines of the Kr laser produced less signal than the shorter-wavelength red lines, the signal produced by the 799·3 nm line being about one-tenth of that produced by the 647·1 and 676·4 nm lines. This result indicates that there must be a dip in the absorption spectrum at around 650 nm, and accordingly the 676·4 nm line of Kr was used for the further studies reported here. The laser line was filtered using a double-prism monochromator of the Claassen *et al* (1969) type in order to eliminate plasma lines from the spectrum, and the power at the sample surface was 60 mW. At higher laser powers, ~100 mW, surface damage was produced through local heating. An argon gas jet was directed at the crystal along the line of the laser beam to help cool the crystal surface and to eliminate the Raman scattering from air. All measurements were carried out at room temperature using a spectral resolution of 3·5 cm^{-1}.

Measurements using the 180°-scattering geometry produced very weak spectra and only one Raman line could be seen: this line was at 100 cm^{-1} and had diagonal polarization. Further measurements were then carried out using the Brewster-angle technique, which maximizes the interaction between the incident light and the highly reflecting

crystal. The technique has been reviewed in detail by Beattie and Gilson (1970) and therefore only the essential points will be given here. The technique is based upon the fact that light incident on a crystal face at Brewster's angle with polarization in the plane of incidence and refraction will enter the crystal with a penetration distance of the order of the wavelength of the light before being completely absorbed. The intensity of the scattered light observed at 90° to the incident light is given by

$$I_{\parallel}^{\alpha\beta} = A[C_{\sigma\sigma}R_{\sigma\sigma} + C_{\tau\tau}R_{\tau\tau} + C_{\sigma\tau}R_{\sigma\tau}]^2 \tag{3}$$

for scattered light polarized in the plane of incidence and scattering and

$$I_{\perp}^{\alpha\beta} = A[C_{\rho\sigma}R_{\rho\sigma} + C_{\rho\tau}R_{\rho\tau}]^2 \tag{4}$$

for scattered light polarized perpendicular to the plane of incidence. The indices α, β refer to crystal directions X, Y and Z, which lie along the a, b and c axes, respectively: β labels the direction along the scattering face in the plane of incidence and α is the direction perpendicular to β, again in the plane of incidence. A is a constant, C a coefficient and R a component of the Raman tensors given in §2: σ, ρ and τ take the meanings x, y or z where appropriate. General expressions for the coefficients C have been given by Beattie and Gilson (1970) and we shall not reproduce them here. Rather, we shall give as an example the case $\alpha = Z, \beta = X$, for which $\sigma = x, \rho = y$ and $\tau = z$, and $C_{xx} = k_c/(1 + n_c^2)$, $C_{zz} = -1/(n_c + n_c^3)$, $C_{xz} = (n_c - k_c)/(n_c + n_c^3)$, $C_{yx} = n_c(1 + n_c^2)^{-1/2}$ and $C_{yz} = -(1 + n_c^2)^{-1/2}$: n_c is the ordinary refractive index for the c direction (we are ignoring the extraordinary ray) and $k_c = (n_c^4 + n_c^2 - 1)^{1/2}$. Similar expressions are readily obtained for the other cases of interest, ($\alpha = X, \beta = Y$) and ($\alpha = X, \beta = Z$).

The refractive index is related to Brewster's angle ϕ by $n = \tan\phi$, and ϕ was measured for $HgIn_2\square Te_4$ by finding the angle at which the reflected component of the 676·4 nm laser line showed a minimum intensity. The results obtained were $\phi_a = 75{\cdot}16 \pm 0{\cdot}30°$ and $\phi_c = 74{\cdot}57 \pm 0{\cdot}31°$, giving $n_a = n_b = 3{\cdot}775 \pm 0{\cdot}015$ and $n_c = 3{\cdot}622 \pm 0{\cdot}015$. Using these values for n_a and n_c, the amplitude coefficients C were calculated for various unique scattering configurations and the results are given in table 3. It must be remembered that these coefficients have to be multiplied by the corresponding Raman tensor component, and the approximate sums of such products squared, in order to obtain the scattering intensities.

Because of the high refractive index, the observed scattered light makes an angle of about 4° with the α direction within the crystal, and the direction of propagation of the

Table 3. Calculated amplitude factors for Brewster-angle scattering.

Scattering configuration	$I_{\parallel}^{ZX}$		$I_{\parallel}^{XY}$		$I_{\parallel}^{XZ}$	
Amplitude factors and symmetries	$C_{xx} = 0{\cdot}961$	$(A_1 + B_1)$	$C_{xx} = -0{\cdot}017$	$(A_1 + B_1)$	$C_{xx} = -0{\cdot}017$	$(A_1 + B_1)$
	$C_{zz} = -0{\cdot}020$	(A_1)	$C_{yy} = 0{\cdot}965$	$(A_1 + B_1)$	$C_{zz} = 0{\cdot}965$	(A_1)
	$C_{xz} = -0{\cdot}195$	(E^{TO})	$C_{yx} = -0{\cdot}190$	(B_2^{TO})	$C_{xz} = 0{\cdot}190$	(E^{LO})
Scattering configuration	$I_{\perp}^{ZX}$		$I_{\perp}^{XY}$		$I_{\perp}^{XZ}$	
Amplitude factors and symmetries	$C_{yx} = 0{\cdot}964$	(B_2^{LO})	$C_{zy} = 0{\cdot}967$	(E^{TO})	$C_{yx} = 0{\cdot}256$	(B_2^{TO})
	$C_{yz} = -0{\cdot}266$	(E^{TO})	$C_{zx} = -0{\cdot}256$	(E^{LO})	$C_{yz} = 0{\cdot}967$	(E^{TO})

phonon involved in the scattering process is at approximately 5·5° to the α direction. Allowing for the finite collection angle for the scattered light, this means that Brewster-angle scattering for this crystal is not far removed from true back scattering. The infrared-active modes are not mixed and there is a clear separation between the transverse and longitudinal waves, as is shown in table 3.

The six definitive spectra obtained from the crystal *a* and *c* faces are shown in figures 5 and 6, where one division on the intensity scale corresponds to a photomultiplier signal of 1000 counts integrated over 60 s. The dips present at about 10 cm^{-1} in the spectra of figures 6(*a*) and (*c*) result from over-occultation by the TTM; 100% transmission is attained by 18 cm^{-1}.

The $I_\perp$ spectra shown in figure 6 contain information about B_2- and E-mode frequencies. As table 3 shows, figure 6(*b*) contains E^{TO+LO} modes only, whereas in figures 6(*a*) and 6(*c*) the B_2^{LO} and E^{TO} modes, respectively, are the dominant features. Figure 6(*a*) shows three B_2^{LO} modes at 74, 152 and 189 cm^{-1} with an additional band at 121 cm^{-1}. This latter band corresponds closely with an E^{TO}-mode frequency, which is allowed in this polarization but may also arise from an impurity, as will be discussed later. Figures 6(*b*) and 6(*c*) show that there are E modes at 42 and 61 cm^{-1} which appear to exhibit no TO–LO splitting. There are E^{TO} modes at 122, $\sim$162 and 181 cm^{-1}, and an E^{LO} mode at $\sim$188 cm^{-1}; the amount of overlap between the three modes in the 100–200 cm^{-1} region makes it difficult to determine all of the frequencies. Although the B_2 and E modes appear only weakly in the Raman spectrum, the B_2^{LO} modes at 152 and 189 cm^{-1} and the E^{TO} modes at 122 and 162 cm^{-1} agree well with the infrared results (see table 2).

The $I_\parallel$ spectra shown in figure 5 are complex because of the variety of modes allowed in each configuration (see table 3). In each spectrum the A_1 modes are dominantly allowed, and the strongest feature at 100 cm^{-1} that was also observed in back scattering can be confidently assigned to A_1 symmetry. B_1 modes are strongly allowed in the configurations $I_\parallel^{ZX}$ and $I_\parallel^{XY}$, and the two weak bands at $\sim$50 and 155 cm^{-1} are tentatively assigned to this symmetry; the low intensity makes it difficult to distinguish these bands, but no corresponding peaks are observed in other configurations where B_1 modes are forbidden or very weakly allowed. It should be noted that the B_1 modes in chalcopyrites, which have a similar crystal structure, are also weak and difficult to observe (Lockwood and Montgomery 1975). Figures 5(*a*) and 5(*b*) also contain peaks from E^{TO} and B_2^{TO} modes, respectively, but this is allowed according to the amplitude factors given in table 3. Figure 5(*c*) shows the $I_\parallel^{XZ}$ spectrum in which the $A_1(R_{zz})$ modes dominate, with a weaker contribution from the E^{LO} modes. The strong 100 cm^{-1} feature is again seen, along with E^{LO} features, and a unique sharp band is evident at 132 cm^{-1}. This latter band appears in no other spectrum, and is therefore assigned to the other A_1 mode. These results indicate that for the 100 cm^{-1} band the Raman tensor component $a \simeq b$, whereas for the 132 cm^{-1} band $b \gg a$.

A strong shoulder is observed on the high-frequency side of the 100 cm^{-1} A_1 band in all of the $I_\parallel$ spectra, accompanied in some cases by the E mode at $\sim$125 cm^{-1}. It was found that when the laser power was increased to the point where surface damage occurred, this shoulder became the dominant feature in the spectrum, peaking at 120 cm^{-1} with an intensity of about twice that of the 100 cm^{-1} band. Simultaneously, two other features of lower intensity appeared at 60 and 141 cm^{-1}, respectively. The Raman spectrum of powdered TeO_2 has three principal bands at 62, 120 and 146 cm^{-1} (Pine and Dresselhaus 1971): these frequencies, and the band intensities, are a good match to the three bands seen here. Furthermore, Pine and Dresselhaus could produce the TeO_2 spectrum by melting Te with a laser beam and then allowing the sample to solidify

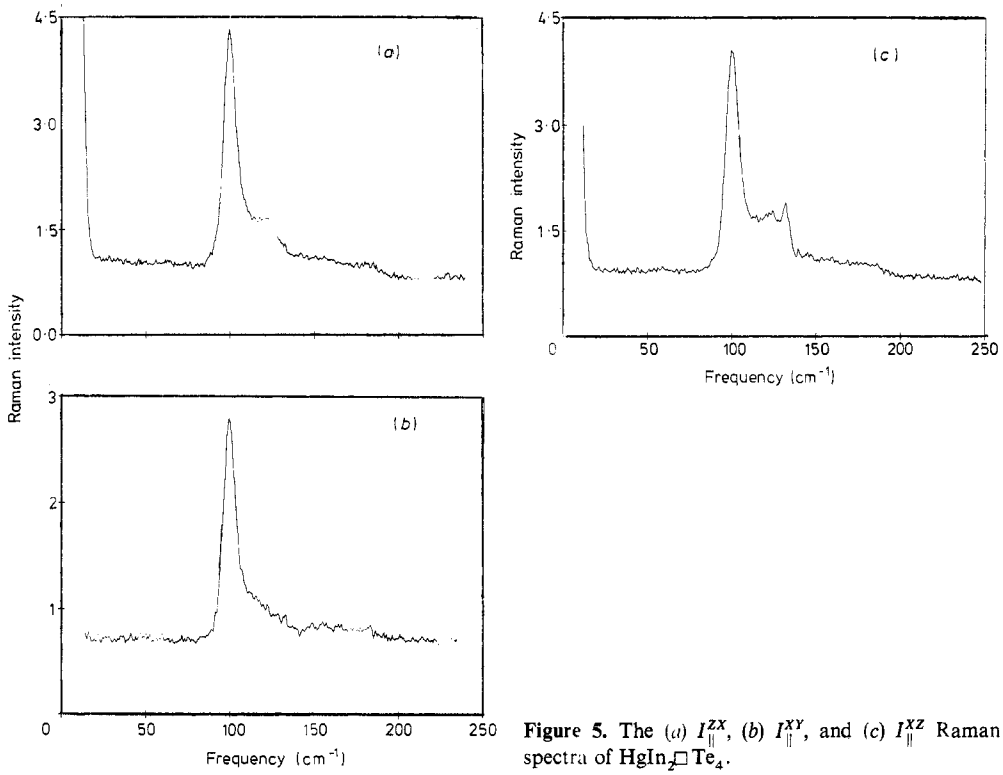

Figure 5. The (*a*) $I_{\parallel}^{ZX}$, (*b*) $I_{\parallel}^{XY}$, and (*c*) $I_{\parallel}^{XZ}$ Raman spectra of $HgIn_2\square Te_4$.

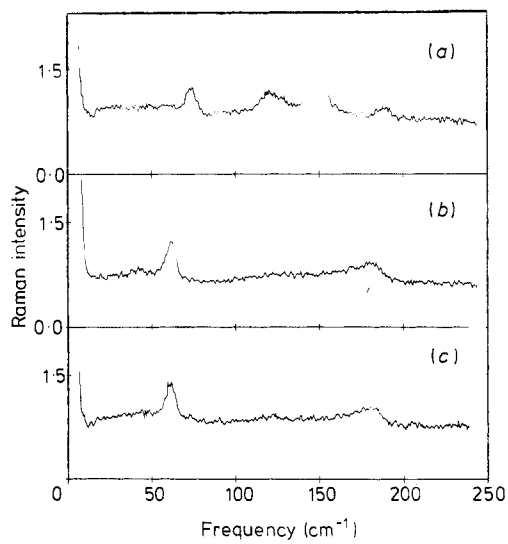

Figure 6. The (*a*) $I_{\perp}^{ZX}$, (*b*) $I_{\perp}^{XY}$, and (*c*) $I_{\perp}^{XZ}$ Raman spectra of $HgIn_2\square Te_4$.

again. These facts indicate that the bands at 60, 120 and 141 cm^{-1} most likely arise from the TeO_2 that is created when the crystal surface is heated. It is probable that some TeO_2 is always present on the surface of the crystal as a result of the grinding and polishing processes. The shoulder feature at $\sim 120\ cm^{-1}$ observed in the $I_{\parallel}$ spectra would then arise from surface scattering by this TeO_2.

5. Theoretical analysis

5.1. Qualitative considerations

It is tempting to apply to the qualitative interpretation of the lattice vibrations in these compounds the simple picture already described in § 2, which has proved useful in the case of various chalcopyrite semiconductors (Holah *et al* 1974). In this picture, the dispersion relations of a zincblende crystal are folded back into the smaller Brillouin zone of the ordered ternary compound so that the zone-centre modes are derived from the modes at certain high-symmetry $\boldsymbol{k}$ points of the zincblende structure (see § 2). However, in the present case, we have the complication of vacant sites and a corresponding reduction in the number of the degrees of freedom of the system relative to the corresponding zincblende crystal. Which of the modes obtained by folding are absent in the correct description? The group representations formed by the vector displacement of a single atom per unit cell decomposes into irreducible representations B_2 and E, which correspond, respectively, to the z and (x, y) components of the displacement. It follows that one B_2 and two E modes are lost when the atom is removed. What is the effect upon the remaining

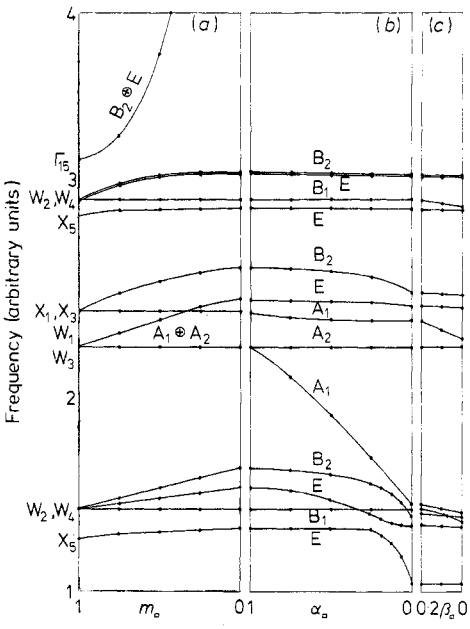

Figure 7. The 'defect diamond' calculation shows the effect of reducing (*a*) the mass on the vacancy site, (*b*) the $\alpha_{\square Te}$ central force constant and (*c*) the $\beta_{Te\square Te}$ bond-bending force constant.

modes of the large perturbation associated with the removal of one atom per cell? One aspect of this problem is illuminated by a simple argument based on the use of bond-*stretching* forces *only*. In zincblende and related semiconductors, one-third of all of the vibrational modes may be identified as those which have zero frequency in the presence of bond-stretching forces only (in zincblende itself these are the TA bands). The number of such modes is obtained by subtraction of the number of bonds per atom (which we constrain to remain constant for such a mode) from the number of degrees of freedom per atom. For an unmodified zincblende structure, the result is $3 - 2 = 1$. If a fraction f of atoms is removed, together with their associated bonds, this becomes $3(1 - f) - 2(1 - 2f) = 1 + f$. In practice, the bond-bending forces are usually small enough for this low-lying group of bands to be clearly identified. The above argument shows that while the total number of modes decreases by a fraction f, the number of these low-lying modes *increases* by the same fraction. In the case of $HgIn_2\square Te_4$ this leads us to expect (at each value of $\boldsymbol{k}$) *one* additional low-lying mode.

The symmetry of the strongly perturbed mode at $\boldsymbol{k} = 0$ may be derived from the following more detailed argument, which is capable of generalization to other cases of interest.

The modes of any structure which have non-zero frequencies in the presence of bond-stretching forces only may be obtained by using the compressions of the bonds, rather than the vector displacements of the atoms, as coordinates. The modification of the zincblende structure to form a defect structure reduces the number of these coordinates by four for each missing atom. One may decompose the group representation formed by the missing coordinates into irreducible representations. Subtraction of the representations associated with the displacement coordinates of the missing atoms themselves then isolates those representations associated with anomalous low-lying modes. In the present case we have $(A_1 + B_2 + E) - (B_2 + E) = A_1$.

The above arguments are illustrated by the calculations shown in figure 7. For simplicity, we have considered the case where one atom in eight is removed from a diamond cubic crystal to form what we shall call 'defect diamond', which is similar to the defect stannite and defect chalcopyrite structures except in that it is made up of identical atoms. We use the simple Keating (1966) model for bond-bending and bond-stretching forces,

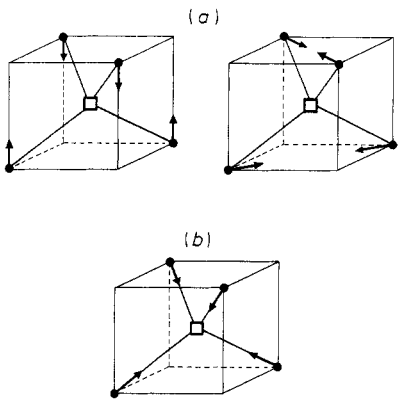

Figure 8.(*a*) The folding of zincblende dispersion relations gives two A_1 modes with displacements in the neighbourhood of the vacancy, as shown. The correct A_1 modes are linear combinations of these. (*b*) As $\alpha_{\square Te}$ is reduced, the displacements of the low-lying A_1 mode discussed in the text take the form shown.

as described in the following section. Figure 7 shows how the $\boldsymbol{k} = 0$ mode frequencies vary as one atom per unit cell is 'switched off' by letting first its mass and then the force constants associated with it tend to zero. In the first stage, a B_2 and a doubly degenerate E mode are lost, as expected, but the spectrum is otherwise only slightly modified. However, when the force constants associated with the defect are cut off, the A_1 mode drops dramatically, as anticipated on the basis of the above analysis. Figure 8 shows the eigenvectors of the A_1 modes before and after the □–Te bonds are cut. It can be seen that the dropping mode primarily involves the stetching of these bonds. Note also that the frequencies of the B_1 and A_2 modes remain constant as the defect mass and defect bond-stretching force constants are taken to zero, since that part of the Hamiltonian which is being changed involves only coordinates which yield A_1, B_2 and E representations.

5.2. Keating-model fit to experimental data

A semi-empirical analysis of the experimental data of §§ 3 and 4, as well as the sound velocities measured by Saunders and Seddon (1976), has been performed using adjustable force constants of the Keating type (Keating 1966, Martin 1970). In the Keating model, the potential energy associated with a given set of atomic displacement is expressed as a sum of two terms which are sums over bonds (corresponding to central nearest-neighbour forces) and pairs of neighbouring bonds (corresponding to non-central forces), respectively.

In the case of an elemental solid, the central force term may be written

$$\tfrac{3}{4}\alpha \sum_{l,\Delta} [(\boldsymbol{u}_l - \boldsymbol{u}_{l\Delta}) \cdot \boldsymbol{r}_\Delta(l)]^2. \tag{5}$$

The summation is over all atoms l and their nearest neighbours $l\Delta$. The unit vector from the equilibrium position of atom l to that of its neighbour $l\Delta$ is $\boldsymbol{r}_\Delta(l)$ and $\boldsymbol{u}_l$ denotes the displacement of atom l.

The non-central force term is

$$\tfrac{3}{16}\beta \sum_{l,\Delta,\Delta'} [(\boldsymbol{u}_l - \boldsymbol{u}_{l\Delta}) \cdot \boldsymbol{r}_{\Delta'}(l) + (\boldsymbol{u}_l - \boldsymbol{u}_{l\Delta'}) \cdot \boldsymbol{r}_\Delta(l)]^2, \tag{6}$$

where the sum is over all atoms l and pairs of nearest neighbours $l\Delta$, $l\Delta'$.

The advantages of the Keating model over alternative short-range force schemes are marginal and, at the level of the analysis undertaken here, insignificant.

In the case of a compound, the above should be modified to incorporate different force constants α for each type of bond, and different β's for each different triad of nearest-

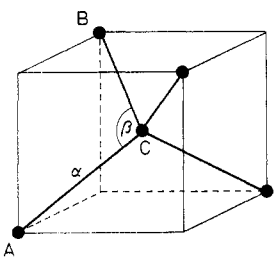

Figure 9. Notation for central (α_{AC}) and non-central (β_{ACB}) Keating model force constants given in table 4.

neighbour atoms. Figure 9 explains the notation which we have used for these various force constants.

In addition, Coulomb forces may be added in the case of a compound. We have ignored this refinement for the present, since the model already contains a considerable number of adjustable constants and is found to give a reasonable fit to the data.

The structure was assumed to be $I\bar{4}2m$, as discussed in § 1, with all atoms placed at their ideal sites (i.e. those coincident with zincblende sites) since there has not yet been an experimental determination of their exact positions.

How one is to treat the vacancy in a model of this type is not clear. The model considers the vacancy as an extra, massless atom which is dealt with in a similar manner to the electron shells in the familiar shell model for ionic solids (Woods *et al* 1960); a force matrix for cores and shells is transformed into a smaller matrix for cores only. In this case a 24 × 24 matrix (i.e. 7 atoms and one vacancy) reduces to a 21 × 21 matrix (i.e. 7 atoms only). In our initial calculations we set the □–Te bond-stretching and Te–□–Te bond-bending force constants equal to zero. However it was found difficult to obtain a satisfactory fit to the data with this restriction and we resorted to the incorporation of a □–Te force constant. This may seem paradoxical but is probably an indication of significant contributions from forces of longer range which are not built into the model.

The theoretical results shown in tables 2 and 5 were obtained with the force constants given in table 4.

As noted above. the lowest A_1 mode is of particular interest. Unfortunately, the associated A_2 mode cannot be observed in either the Raman or infrared reflectivity measurements, but it seems clear that the A_1 mode frequency in question is not lowered through the presence of the vacancy by as much as our previous argument would suggest. Indeed, this is one the reasons for the necessity of the incorporation of the □–Te force constant in the model.

Table 4. Keating model parameters required for results in table 2.

Force constant		Fitted value ($N\,m^{-1}$)
α	Hg–Te	38·9
	In–Te	21·8
	□–Te	11·8
β	In–Te–In	2·95
	In–Te–Hg	2·95
	Te–In–Te	2·95
	Te–Hg–Te	2·95
	□–Te–In	1·47
	□–Te–Hg	1·47
	Te–□–Te	0·0

Table 5. Experimental and calculated values of elastic stiffness constants (C) and bulk modulus (B) ($\times 10^{10}\,N\,m^{-2}$).

	C_{11}	C_{12}	C_{13}	C_{33}	C_{44}	C_{66}	B
Experimental	4·31	2·54	2·18	4·47	2·14	2·41	2·99
Calculated	4·2	2·88	2·9	4·4	1·18	1·21	3·35

The degree of agreement with experiment thus achieved is sufficient for present purposes—to assist in the preliminary identification and interpretation of the data. It is least satisfactory for the 147 cm^{-1} B_2 mode, the 120 cm^{-1} E mode and the C_{13}, C_{44} and C_{66} elastic constants.

Dispersion relations were calculated for various symmetry directions and are shown in figure 10.

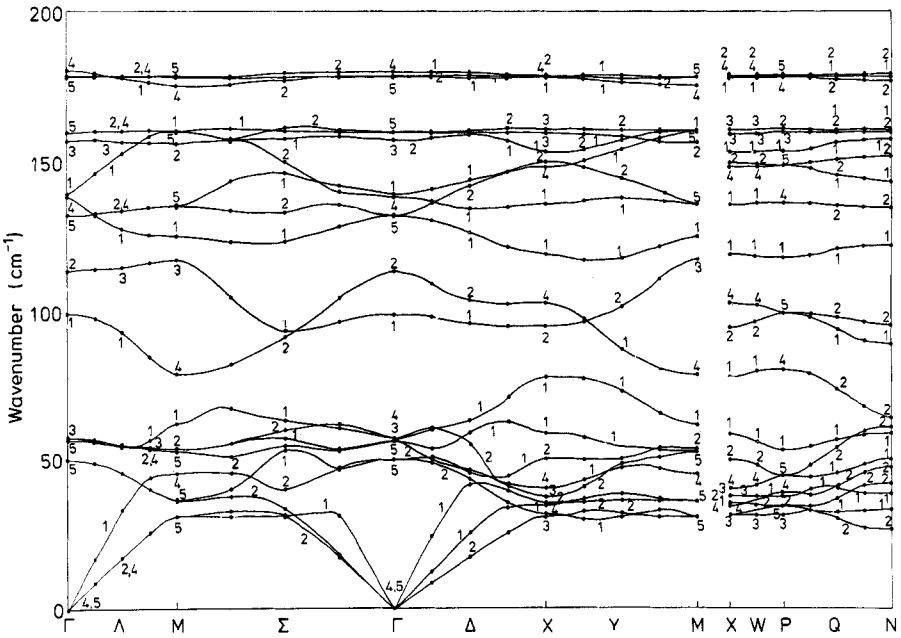

Figure 10. Phonon dispersion curves of $HgIn_2\square Te_4$ calculated using the fitted Keating model parameters.

6. Conclusions

The ordered vacancy compounds, of which $HgIn_2\square Te_4$ is a particularly simple example, pose many intriguing questions, most of them bearing on the role of the vacancies. For example, in many of these compounds, the arrangement of vacancies is disordered above a certain transition temperature. A little thought will suffice to convince the reader that this is not so straightforward a proposition as the disorder in a solid solution; in the defect case, one is dealing with a situation in which a large fraction of the cation sites are unfilled!

In addition, there is at present wide interest in the possible merits of the chalcopyrite semiconductors in various technical applications. This can be expected to widen to include the ordered vacancy compounds, some of which are in many respects similar to the chalcopyrites.

Clearly, therefore, these compounds invite further attention and it is hoped that this paper may serve to lay some of the groundwork for future investigations.

Acknowledgments

We are indebted to G Saunders for much advice and encouragement and for making available to us the crystals, grown by T Seddon and himself, upon which our measurements were performed. We wish also to thank H Vass for technical assistance in the Raman scattering work, N S J Kennedy for checking the crystal orientation and B S Wherrett for his advice on the group theoretical aspects of our investigation. This work was supported by the Science Research Council.

References

Arthur J W and Lockwood D J 1974 *J. Raman Spectrosc.* **2** 53–69
Beattie I R and Gilson T R 1970 *J. Chem. Soc.* (A) 980–6
Bettini M 1975 *Phys. Stat. Solidi* (b) **69** 201–12
Claassen H H, Selig H and Shamir J 1969 *Appl. Spectrosc.* **23** 8–12
Finkman E, Tauc J, Kershaw P and Wold A 1975 *Phys. Rev.* B **11** 3785–94
Hahn H, Frank G, Klinger W, Störger A D and Störger G 1955 *Z. Anorg. Allg. Chem.* **279** 241–70
Holah G D, Webb J S and Montgomery H 1974 *J. Phys. C: Solid St. Phys.* 7 3875–90
Keating P N 1966 *Phys. Rev.* **145** 637–45
Lax M J 1974 *Symmetry Principles in Solid State and Molecular Physics* (New York: Wiley) p 449
Lockwood D J and Montgomery H 1975 *J. Phys. C: Solid St. Phys.* **8** 3241–50
Lyddane R H, Sachs R G and Teller E 1941 *Phys. Rev.* **59** 673–6
Martin R M 1970 *Phys. Rev.* B **1** 4005–11
Parthé E 1964 *Crystal Chemistry of Tetrahedral Structures* (New York: Gordon and Breach) pp 46–86
Peckham G 1970 *Computer J.* **13** 418
Pine A S and Dresselhaus G 1971 *Phys. Rev.* B **4** 356–71
Saunders G A and Seddon T 1970 *J. Phys. Chem. Solids* **31** 2495–504
—— 1976 *J. Phys. Chem. Solids* to be published
Woods A D B, Cochran W and Brockhouse B N 1960 *Phys. Rev.* **119** 980–99